

# RECONSTRUCTION OF VEES, KINKS, $\Xi^-$ 's, and $\Omega^-$ 's IN THE FOCUS SPECTROMETER

The FOCUS Collaboration

J. M. Link <sup>a</sup>, M. Reyes <sup>a,1</sup>, P. M. Yager <sup>a</sup>, J. C. Anjos <sup>b</sup>,  
I. Bediaga <sup>b</sup>, C. Göbel <sup>b,2</sup>, J. Magnin <sup>b</sup>, A. Massafferri <sup>b</sup>,  
J. M. de Miranda <sup>b</sup>, I. M. Pepe <sup>b,3</sup>, A. C. dos Reis <sup>b</sup>, S. Carrillo <sup>c</sup>,  
E. Casimiro <sup>c,4</sup>, E. Cuautle <sup>c,5</sup>, A. Sánchez-Hernández <sup>c</sup>,  
C. Uribe <sup>c,6</sup>, F. Vázquez <sup>c</sup>, L. Cinquini <sup>d,7</sup>, J. P. Cumalat <sup>d</sup>,  
B. O'Reilly <sup>d</sup>, J. E. Ramirez <sup>d</sup>, E. W. Vaandering <sup>d,8</sup>,  
J. N. Butler <sup>e</sup>, H. W. K. Cheung <sup>e</sup>, I. Gaines <sup>e</sup>,  
P. H. Garbincius <sup>e</sup>, L. A. Garren <sup>e</sup>, E. Gottschalk <sup>e</sup>,  
P. H. Kasper <sup>e</sup>, A. E. Kreymer <sup>e</sup>, R. Kutschke <sup>e</sup>, S. Bianco <sup>f</sup>,  
F. L. Fabbri <sup>f</sup>, S. Sarwar <sup>f</sup>, A. Zallo <sup>f</sup>, C. Cawfield <sup>g</sup>,  
D. Y. Kim <sup>g</sup>, A. Rahimi <sup>g,9</sup>, J. Wiss <sup>g</sup>, R. Gardner <sup>h</sup>,  
A. Kryemadhi <sup>h</sup>, Y. S. Chung <sup>i,10</sup>, J. S. Kang <sup>i</sup>, B. R. Ko <sup>i</sup>,  
J. W. Kwak <sup>i</sup>, K. B. Lee <sup>i,11</sup>, H. Park <sup>i,12</sup>, G. Alimonti <sup>j</sup>,  
M. Boschini <sup>j</sup>, P. D'Angelo <sup>j</sup>, M. DiCorato <sup>j</sup>, P. Dini <sup>j</sup>,  
M. Giammarchi <sup>j</sup>, P. Inzani <sup>j</sup>, F. Leveraro <sup>j</sup>, S. Malvezzi <sup>j</sup>,  
D. Menasce <sup>j</sup>, M. Mezzadri <sup>j</sup>, L. Milazzo <sup>j</sup>, L. Moroni <sup>j</sup>,  
D. Pedrini <sup>j</sup>, C. Pontoglio <sup>j</sup>, F. Prelz <sup>j</sup>, M. Rovere <sup>j</sup>, S. Sala <sup>j</sup>,  
T. F. Davenport III <sup>k</sup>, L. Agostino <sup>l,13</sup>, V. Arena <sup>l</sup>, G. Boca <sup>l</sup>,  
G. Bonomi <sup>l,14</sup>, G. Gianini <sup>l</sup>, G. Liguori <sup>l</sup>, M. M. Merlo <sup>l</sup>,  
D. Pantea <sup>l,15</sup>, S. P. Ratti <sup>l</sup>, C. Riccardi <sup>l</sup>, I. Segoni <sup>l,13</sup>,  
P. Vitulo <sup>l</sup>, H. Hernandez <sup>m</sup>, A. M. Lopez <sup>m</sup>, H. Mendez <sup>m</sup>,  
L. Mendez <sup>m</sup>, E. Montiel <sup>m</sup>, D. Olaya <sup>m,13</sup>, A. Paris <sup>m</sup>,  
J. Quinones <sup>m</sup>, C. Rivera <sup>m</sup>, W. Xiong <sup>m</sup>, Y. Zhang <sup>m,16</sup>,  
J. R. Wilson <sup>n</sup>, K. Cho <sup>o,12</sup>, T. Handler <sup>o</sup>, R. Mitchell <sup>o</sup>,  
D. Engh <sup>p</sup>, M. Hosack <sup>p</sup>, W. E. Johns <sup>p</sup>, M. Nehring <sup>p,17</sup>,  
P. D. Sheldon <sup>p</sup>, K. Stenson <sup>p</sup>, M. Webster <sup>p</sup>, M. Sheaff <sup>q</sup>

<sup>a</sup>University of California, Davis, CA 95616

<sup>b</sup>Centro Brasileiro de Pesquisas Físicas, Rio de Janeiro, RJ, Brasil

- <sup>c</sup>*CINVESTAV, 07000 México City, DF, Mexico*
- <sup>d</sup>*University of Colorado, Boulder, CO 80309*
- <sup>e</sup>*Fermi National Accelerator Laboratory, Batavia, IL 60510*
- <sup>f</sup>*Laboratori Nazionali di Frascati dell'INFN, Frascati, Italy I-00044*
- <sup>g</sup>*University of Illinois, Urbana-Champaign, IL 61801*
- <sup>h</sup>*Indiana University, Bloomington, IN 47405*
- <sup>i</sup>*Korea University, Seoul, Korea 136-701*
- <sup>j</sup>*INFN and University of Milano, Milano, Italy*
- <sup>k</sup>*University of North Carolina, Asheville, NC 28804*
- <sup>l</sup>*Dipartimento di Fisica Nucleare e Teorica and INFN, Pavia, Italy*
- <sup>m</sup>*University of Puerto Rico, Mayaguez, PR 00681*
- <sup>n</sup>*University of South Carolina, Columbia, SC 29208*
- <sup>o</sup>*University of Tennessee, Knoxville, TN 37996*
- <sup>p</sup>*Vanderbilt University, Nashville, TN 37235*
- <sup>q</sup>*University of Wisconsin, Madison, WI 53706*

---

## Abstract

We describe the various techniques developed in the Fermilab Wideband Experiments, E687 and FOCUS, to reconstruct long-lived states. The techniques all involve modifications to standard tracking techniques and are useful to report for future experiments.

---

## 1 Introduction

FOCUS is a photoproduction experiment located at Fermilab which has been configured to investigate the production and decay of charmed particles. As charmed particles typically decay to states containing strange particles, techniques have been developed to reconstruct long-lived mesons and baryons containing strange quarks. The techniques employ a full range of information from a multipurpose spectrometer including partially reconstructed tracks and kinematic constraints, and utilize excellent charged particle identification using Čerenkov detectors, efficient muon identification, and the ability to reconstruct neutral hadronic energy.

In this paper we will briefly describe the spectrometer in Section 2. In Section 3 we will discuss how the tracking is performed in the silicon microstrip detector and in the multiwire proportional chambers and how the individual segments are linked to form tracks. In Section 4 we describe our neutral Vee reconstruction techniques. In Section 5 we present our algorithms for identifying  $\Sigma$  decays where one decay product goes undetected (Kinks). In Section

---

<sup>1</sup> Present Address: Instituto de Física y Matemáticas, Universidad Michoacana de San Nicolás de Hidalgo, Morelia, Mich., Mexico 58040

<sup>2</sup> Present Address: Instituto de Física, Facultad de Ingeniería, Univ. de la República, Montevideo, Uruguay

<sup>3</sup> Present Address: Instituto de Física, Universidade Federal da Bahia, Salvador, Brazil

<sup>4</sup> Present Address: INFN sezione di Milano, Milano, Italy

<sup>5</sup> Present Address: Instituto de Ciencias Nucleares, Universidad Nacional Autónoma de México. CP 04510. México

<sup>6</sup> Present Address: Instituto de Física, Universidad Autónoma de Puebla, Puebla, México

<sup>7</sup> Present Address: National Center for Atmospheric Research, Boulder, CO

<sup>8</sup> Present Address: Vanderbilt University, Nashville, TN 37235

<sup>9</sup> Present Address: Intel Corporation, Portland Technology Development, RA1-238 5200 N.E. Elam Young Parkway Hillsboro, OR 97124

<sup>10</sup> Present Address: University of Rochester, Fermilab, P.O. Box 500, Batavia, IL 60510

<sup>11</sup> Present Address: Korea Research Institute of Standards and Science, P.O.Box 102, Yusong-Ku, Taejeon 305-600, South Korea

<sup>12</sup> Present Address: Center for High Energy Physics, Kyungpook National University, 1370 Sankyok-dong, Puk-ku, Taegu, 702-701, Korea

<sup>13</sup> Present Address: University of Colorado, Boulder 80309

<sup>14</sup> Present Address: Dipartimento di Chimica e Fisica per l'Ingegneria e per i Materiali, Università di Brescia and INFN sezione di Pavia

<sup>15</sup> Present Address: Nat. Inst. of Phys and Nucl. Eng., Bucharest, Romania

<sup>16</sup> Present Address: Lucent Technology

<sup>17</sup> Present Address: Adams State College, Alamosa, CO 81102

6 we present our methods for combining of the Vee and Kink algorithms to find  $\Xi^-$  and  $\Omega^-$  decays.

## 2 Spectrometer Components and Layout

The spectrometer shown in Fig. 1 consists of two dipole magnets, M1 and M2; a 12 plane silicon microstrip array; five stations of multiwire proportional chambers; 300 threshold Čerenkov cells arranged in three gas boxes; two electromagnetic calorimeters for photon, electron, and  $\pi^0$  reconstruction; two muon detectors; and a hadronic calorimeter for triggering and neutral hadron reconstruction. There are 10 meters along the spectrometer in which Vees can be reconstructed. There is also a large charged particle acceptance covering the entire forward hemisphere. The FOCUS spectrometer is an upgraded version of the previous experiment E687. A detailed description of the E687 spectrometer and its performance may be found in Reference 1.

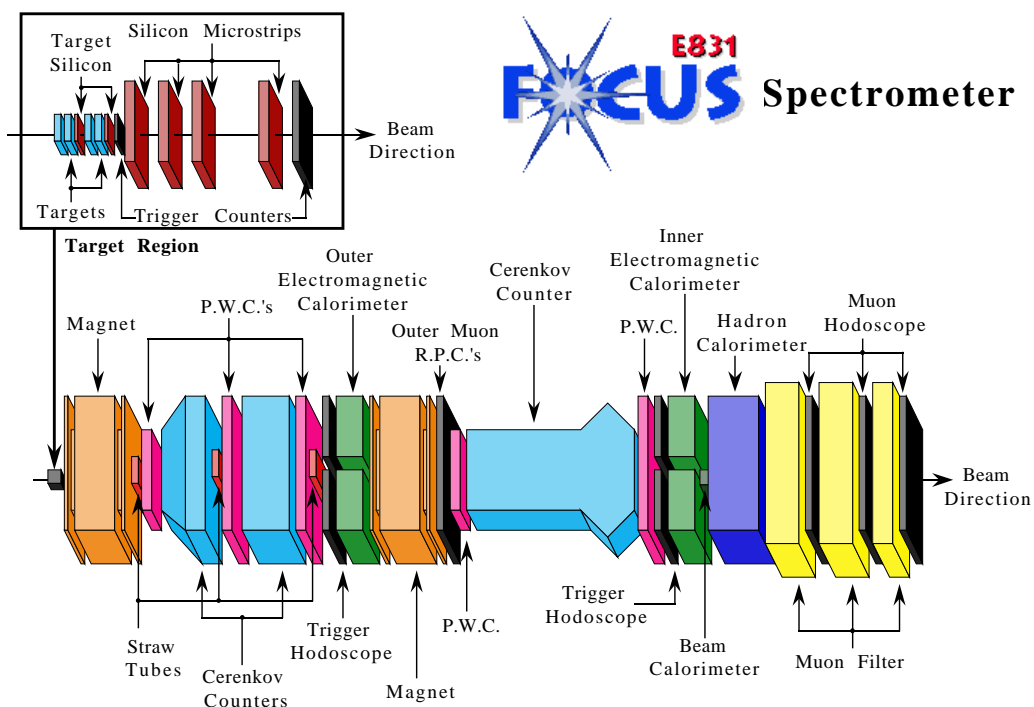


Fig. 1. A schematic drawing of the FOCUS spectrometer. The inset displays the segmented targets, the embedded target silicon, the trigger counters, and the 12 plane silicon tracking array. The spectrometer is about 30 meters long.

The two large aperture magnets are used to momentum analyze charged tracks. The magnets are oriented to bend particles in the vertical ( $y$ -axis) direction with M1 and M2 bending in *opposite* directions. Positive particles

are bent upwards in M1. The particular arrangement of magnet positions and orientation was chosen for its unique effect on event topology. There is a large background of  $e^+e^-$  pairs coming from beam photon conversions in the experimental target. Pairs are produced with little transverse momentum with respect to the beam direction ( $z$  direction) and with a transverse profile comparable to the beam size (about 1 cm in  $x$  and  $y$ ). The first magnet bends the electrons and positrons in  $y$ , creating a vertical swath. The lowest energy pairs strike the inside of M1 or the upstream face of M2, while the remainder pass through the M2 aperture and are bent back towards the beam axis. The beam profile is reconstituted at the end of the spectrometer, with some smearing due to energy loss via bremsstrahlung from material throughout the spectrometer.

The target is composed of segmented BeO slabs with silicon microstrip doublets after the first two targets and after the last two targets. For historical reasons these four silicon microstrip planes are not used directly in the track reconstruction, however they are used to extend the microstrip tracks to the production and secondary vertices. By making a measurement close to the vertex we are able to improve both the position and the angular resolution of the track.

### 3 Standard Tracking Devices and Algorithms

#### 3.1 Microstrip Detector

The high resolution tracking of charged particles provided by the Silicon microStrip Detector, or the SSD, is essential to the reconstruction of charmed particle decay vertices and in separating these vertices from the production vertex.

The SSD consists of four physically separated stations with three planes per station. The three planes of each station are oriented to  $i$ ,  $j$ , and  $k$  coordinates of -135, -45, and -90 degrees with respect to the horizontal ( $x$  axis). The microstrip detector and target layout is shown in Fig. 2 and a detailed summary of the active area, high resolution region, strip pitch, and number of channels for each station is given in Table 1.

The innermost section of each plane, covering the region where tracks pass most closely to each other, has twice the resolution of the outer section. In addition, the most upstream station has a resolution twice as good as the other stations. Pulse heights are read out for all 8,256 strips. The overall detection efficiency of each plane is better than 99% even including the non-functioning strips and broken electronics channels. A more complete description of this

detector and its performance can be found in Reference 2.

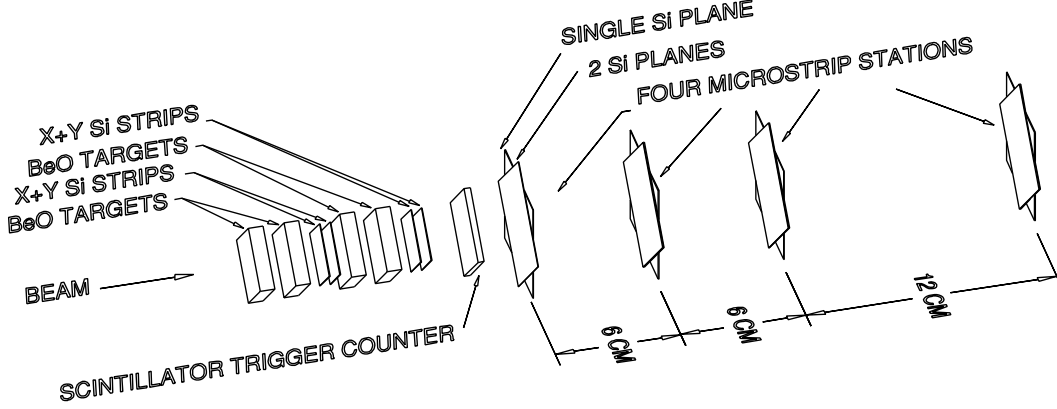


Fig. 2. A layout drawing of the silicon microstrip detector together with the BeO production targets and embedded target silicon strip planes.

The microstrip tracking algorithm is based on projection finding using hits in three separate views. A hit is a cluster of one to three adjacent strips depending on the summed pulse heights in the strips (less than a 1.5 minimum ionizing pulse height) and on the number of neighboring strips with pulse heights above threshold. As momentum information is not yet available multiple Coulomb scattering effects are not considered. Projections are found using very loose selection criteria. At least three hits per view (out of a possible four) are required and sharing of hits is permitted. Hits in the last three stations that are already assigned to a projection having hits in all four stations cannot be reused for a new projection containing only three hits. Projections are combined to form tracks if they match in space with a global  $\chi^2$  per degree of freedom less than 8. Tracks sharing projections are arbitrated according to their  $\chi^2$ . The process is performed in a fully symmetric way with respect to the views.

The pulse height information on each hit is used in three ways. First, the information allows for the separation of two overlapping hits in the pattern recognition. Second, the pulse height information is combined from all hits in the SSD in the track to determine whether the track is consistent with the passage of a singly charged track through the planes. By requiring more than 1.5 times a standard singly charged pulse height we can identify  $e^+e^-$  pairs. Third, and most importantly, we use the charge sharing between neighboring strips to obtain an improved position resolution.

Table 1

Properties of the Silicon Microstrip Detector. The first three lines are the internal relative z locations of the silicon microstrip planes.

Property	I station	II station	III station	IV station
1 <sup>st</sup> detector	-0.5 cm	5.5 cm	11.5 cm	23.5 cm
2 <sup>nd</sup> detector	0.0 cm	6.0 cm	12.0 cm	24.0 cm
3 <sup>rd</sup> detector	0.5 cm	6.5 cm	12.5 cm	24.5 cm
active area	$2.5 \times 3.5 \text{ cm}^2$	$5 \times 5 \text{ cm}^2$	$5 \times 5 \text{ cm}^2$	$5 \times 5 \text{ cm}^2$
high res area	$1.0 \times 3.5 \text{ cm}^2$	$2 \times 5 \text{ cm}^2$	$2 \times 5 \text{ cm}^2$	$2 \times 5 \text{ cm}^2$
strip pitch	25 $\mu\text{m}$ , 50 $\mu\text{m}$	50 $\mu\text{m}$ , 100 $\mu\text{m}$	50 $\mu\text{m}$ , 100 $\mu\text{m}$	50 $\mu\text{m}$ , 100 $\mu\text{m}$
# of channels	$688 \times 3$	$688 \times 3$	$688 \times 3$	$688 \times 3$

### 3.2 Multiwire Proportional Chambers (MWPCs)

Five stations of Multiwire Proportional Chambers are used to track charged particles in the main spectrometer. The first three chamber stations, labelled P0, P1, and P2, are located between the two analyzing magnets, M1 and M2. The other two chamber stations, P3 and P4, are located downstream of the second magnet, M2. This arrangement allows for two momentum measurements for higher energy tracks which pass through both magnets as well as providing momentum information for wide angle tracks which are not accepted by the M2 aperture.

Each of the chamber stations consist of four planes of wires, measuring  $y$ ,  $u$ ,  $v$ , and  $x$  positions. The X-view wires, running vertically, measure the horizontal (non-bend view) position. The U-view and V-view wires are oriented at  $\pm 11.3$  degrees with respect to the Y-view, an arrangement which is used to resolve ambiguities and to provide better momentum resolution.

The tracking algorithm for the multiwire proportional chambers is used to reconstruct spectrometer tracks which have the first hit in P0 (the most upstream chamber) and which extend into at least one additional chamber. As with microstrip tracks, a projection finding algorithm is used. The X-view is special because it is the only MWPC view in which the charged particles are not bent.

First a microstrip track is extended into the non-bend X-view of the chambers. A search is made for MWPC hits which match this “seed” projection. Next, projections are formed from hits in the U-view, V-view, and Y-view. The projections in all four views are combined to form tracks. Further X-view

projections are formed using unused MWPC hits where no seed track exists and these projections are also matched with unused U-view, V-view, and Y-view projections to reconstruct additional tracks. Tracks are required to extend through at least the first three MWPCs. A least squares fit is performed on all candidate tracks. The fit parameters are the intercepts and slopes of the track in the  $xz$  and  $yz$  planes. If a track passes through just the first three MWPCs, then it is referred to as a *stub*. For tracks passing through all five chamber stations (called 5-chamber tracks or just *tracks*), the change in the  $y$  slope between the track segments upstream and downstream of M2, *i.e.* the bend angle, is an additional parameter.

An approximate momentum is assigned to 5-chamber tracks by using the bend angle in M2 and the sudden bend approximation. Various magnetic corrections are applied to this category of tracks. Fringe fields in M1 and M2, extending beyond the magnetic poles, and off-field components of the magnetic field ( $B_y$  and  $B_z$ ) are treated by higher order corrections to the linear fit. The corrections are applied by iterating each 5-chamber track through a complete fit which includes the magnetic corrections. The track momentum is adjusted appropriately after each iteration.

### 3.3 Linking

Once tracks are reconstructed in the silicon microstrip and MWPC systems, they must be linked together to determine which microstrip track is associated to which MWPC track. This is accomplished by extrapolating each microstrip track to the center of M1 and searching for MWPC tracks which, when extrapolated back to this same point in  $z$ , “match” with it. This matching is performed by comparing the MWPC track’s extrapolated  $x$  slope and  $x$  intercept at the center of M1 with the same quantities for the microstrip track in question. Because the magnetic field is in the  $x$  direction there is no (or little) bending of charged tracks in this view. Thus, for a MWPC track and a microstrip track created by the same particle these two  $x$  quantities should agree. (This match is accomplished after a correction is made for weak focusing in the non-bend view.) A global least squares fit using all the hit information from the microstrip segment and the MWPC segment is then performed on each candidate. Multiple MWPC segments linked to the same microstrip segment are arbitrated on the basis of the  $\chi^2$  per degree of freedom of the fit. A maximum of two MWPC tracks are allowed to be linked to the same microstrip track. This decision is made because  $e^+e^-$  pairs from beam photon conversions frequently reconstruct as a single microstrip track due to their extremely small opening angles, but will reconstruct as two separate MWPC tracks as the  $e^+$  and  $e^-$  are bent in opposite directions in M1.



Track segments from the microstrip tracks and the MWPC tracks which fail to link are used to form Vees, Kinks,  $\Xi^-$ 's, and  $\Omega^-$ 's.

### 3.4 Primary Vertex

In the early stages of data reconstruction a basic vertex algorithm is implemented using only the microstrip track information. These vertices are used for reconstructing different Vee categories and are meant to be roughly correct. Later in our analyses the “true” primary vertex is recalculated using all available tracking information with multiple scattering information included. The exact algorithm depends on the final state that is being investigated. For instance we use a candidate driven approach when the decay daughters are fully reconstructed such as  $D^0 \rightarrow K^- \pi^+$ , a special seed plane approach for one prong final states such as  $D^+ \rightarrow K_S^0 \pi^+$ , and a stand alone vertexing algorithm for semileptonic decays such as  $D^+ \rightarrow K^- \pi^+ \mu^+ \nu$ . These techniques have been described in several E687 theses. A good reference is the thesis [3] of Luca Cinquini.

The basic vertex algorithm minimizes the distance of closest approach of the tracks in the transverse plane. Specifically, the minimized quantity is:

$$\chi^2 = \sum_{i=1}^n \left( \frac{X - (x_i + a'_i Z)}{\sigma_{x,i}} \right)^2 + \left( \frac{Y - (y_i + b'_i Z)}{\sigma_{y,i}} \right)^2 \quad (1)$$

where X, Y, Z are the coordinates of the vertex taken from the parameters of the fit,  $a'_i, b'_i, x_i, y_i$  are the slopes and intercepts of the i-th track, and  $\sigma_{x,i}, \sigma_{y,i}$  are the errors returned by the purely geometric track fit to the hits of the i-th track.

The algorithm begins by assigning all microstrip tracks to a common vertex and by computing the corresponding  $\chi^2$ . Tracks are removed from this vertex one at a time, beginning with the one that gives the largest contribution to the  $\chi^2$ . Each time the vertex is refit and the subtraction process continues until the  $\chi^2$  falls below the threshold. Since the space location may have changed in the process, all discarded tracks are individually tested to check whether they originate from the found vertex and if so, they are included. Once the construction of the first vertex is completed, the procedure is repeated with the remaining set of tracks. At the end of the process each microstrip track is assigned to just one vertex, or they might remain unassigned. For Vee finding algorithms the most upstream microstrip vertex within the target is called the primary vertex. If no primary vertex is found, then the center of the target is selected as the primary vertex.

#### 4 Vees

$K_S^0$  and  $\Lambda^0$  (usually referred to as “Vees”) are often found among the decay products of charmed particles. In FOCUS, these particles are reconstructed through the charged decay modes [4]:

$$\begin{aligned} K_S^0 &\rightarrow \pi^+ \pi^- (\text{BR} = 68.6\%) \\ \Lambda^0 &\rightarrow p \pi^- (\text{BR} = 63.9\%) \end{aligned}$$

These particles are relatively long-lived with respect to charmed particles, and may travel several meters in the spectrometer before decaying. Depending on the region of decay, they leave topologically distinct tracks, but they must be reconstructed with different algorithms. In all, Vees can be reconstructed in the FOCUS spectrometer over a decay length of about 10 meters. A sketch of the regions where different algorithms are employed for Vee reconstruction is presented in Fig. 3.

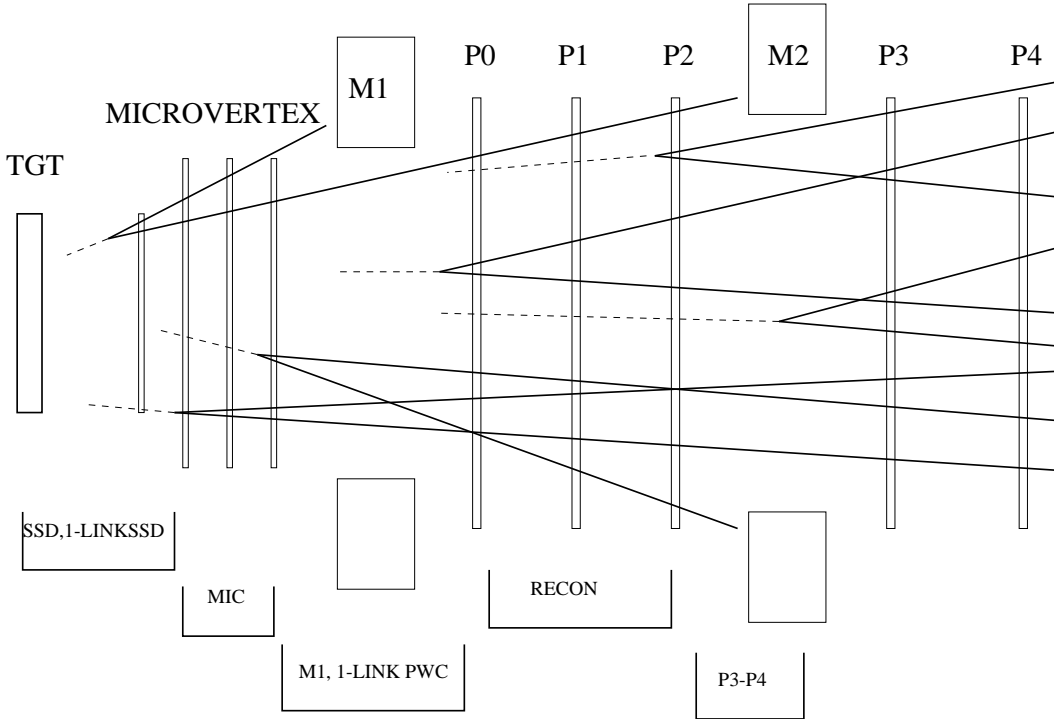


Fig. 3. A schematic drawing of the regions of the spectrometer in which Vees are reconstructed by different algorithms. The solid lines are the two-prong daughter products of the Vees. The dashed lines indicate that the parent particle originated from the target region. Note that target box (TGT) is simply for illustration. In the experiment it is segmented and interleaved with silicon planes.

All Vee-reconstruction codes have in common the search for a pair of oppositely charged tracks which originate from a common point in space, the Vee decay vertex. The invariant mass of the pair is computed by first assigning the pion

mass to both tracks to test the  $K_S^0$  hypothesis. Next, the proton mass is assigned to the faster particle and the pion mass to the slower particle to check for a  $\Lambda^0$ . Initially, there is no Čerenkov identification applied, and the Vee requirements are intentionally left loose to allow for different degrees of signal to noise in individual analyses.

While not all Vee categories were used in FOCUS analyses, we did develop algorithms to identify and to reconstruct Vees in all regions described in this section. The SSD Vees, M1 Vees, and One-link SSD Vees were used in several analyses. The RECON Vee and P34 Vee categories were used in E687, but were not implemented in FOCUS. This resulted from a reduction in the beam energy such that long-lived decays became relatively less important. It is also the result of running the beam at much higher intensity which led to increased noise in the chambers which in turn made the rate of false RECON Vees high and the algorithm less efficient. For a similar reason the MIC Vee algorithm was implemented in E687, but not in FOCUS. All MIC Vees are first found as M1 Vees and it required excessive computer time to search over all the remaining microstrip hits. Finally, the Single-linked MPWC Vees were only used in searching for  $\Xi^-$  and  $\Omega^-$  decays.

#### 4.1 SSD Vees

SSD Vees are reconstructed from pairs of oppositely charged linked SSD-MPWC tracks originating from a common vertex. As the decays in this category occur close to the primary vertex, they tend to be lower momentum and accordingly have an excellent mass resolution. These decays are principally  $K_S^0$  and  $\Lambda^0$  which decay upstream of the second SSD station. The secondary Vee vertex is required to lie downstream of the reconstructed SSD primary vertex. Basically, these Vees are found in the same way [5] that we find charm particles. As such if matching hits are found in the target silicon planes then they are added into the silicon track definition. The SSD Vees are the cleanest and the best defined category of Vees: the Vee track for this category has a resolution comparable to that of two combined SSD tracks. The standard deviations for the  $K_S^0$  and  $\Lambda^0$  mass distributions in this category are  $3.6 \text{ MeV}/c^2$  and  $1.6 \text{ MeV}/c^2$  respectively.

#### 4.2 M1 Vees

The M1 Vees are composed of  $K_S^0$  and  $\Lambda^0$  which decay between the last SSD plane and the first MPWC station, P0. They are reconstructed with pairs of unlinked MPWC tracks and are divided in three subcategories, according to the nature of their components: *track-track*, *track-stub*, and *stub-stub*.

The reconstruction algorithm is substantially the same for the three topologies. For each candidate pair of unlinked MPWC tracks, the intersection in the  $xz$  plane (non-bend) is first found; an iterative procedure then traces the two prongs through the M1 field and determines the  $y$  location of the Vee vertex. In the case of a track-stub Vee, the tracing also allows the computation of the unknown momentum and charge of the stub prong. For a stub-stub Vee, it is necessary to further constrain the Vee vector to originate from the SSD primary vertex and then the unknown momenta can be computed. Finally, a global fit using the full covariance matrices of the tracks (including multiple Coulomb scattering effects) is applied to each Vee candidate to provide a better estimate of the Vee decay vertex and the Vee momentum.

M1 Vees are the most copious Vee category, accounting for over 70% of the total reconstructed Vee sample. Their mass resolution and vertex resolution are not as good as for the SSD Vees and are a very strong function of the angle that the M1 field makes with respect to the normal of the Vee decay plane. The resultant mass distributions often have very non-Gaussian tails. To correct for this effect, Vees are retained based on a normalized mass cut or the difference between the reconstructed and nominal Vee mass divided by the anticipated resolution for a given topology. The normalized mass distribution is much closer to a true Gaussian distribution. Our selection criteria for the M1 Vees is that the absolute value of the normalized mass be less than 5. The  $K_S^0$  mass resolution for the M1 Vee category varies from 6.6 MeV/ $c^2$  for *stub-stub* Vees to 5.9 MeV/ $c^2$  for *track-track* Vees.

### 4.3 RECON Vees

RECON Vees are Vees which decayed between P0 and P2. Because their decay region is further downstream, they tend to be a Vee category with higher momentum.

RECON Vees are reconstructed using hits in P1, P2, P3, and P4 which have not already been used by the general MPWC pattern recognition (which only finds tracks with hits in P0). This requirement significantly speeds up the algorithm, but it reduces the efficiency in higher multiplicity events. First, track projections in the  $xz$  (non-bend) view are constructed and checked two at a time for intersecting between P0 and P2. Projections which do not intersect in the desired region with any other projection view are disregarded. Then, projections in the U-view, V-view, and Y-view are formed and matched to the  $xz$  plane projections to form tracks in space, with only loose requirements on the  $\chi^2/\text{DOF}$  of the track. Several track topologies are allowed: P1234 (*i.e.* tracks with hits in P1, P2, P3, and P4), P123, P234, and P23. Finally, tracks are combined pairwise and a global fit to the Vee hypothesis is performed. The

parameters of the fit are the five parameters for each track ( $x$  and  $y$  slopes and intercepts and the  $y$  bend angle in M2) plus the coordinates of the Vee vertex. In the case of P23 candidates (for which prongs are defined by a single point on each side of the magnet) it is also necessary to assume that the Vee originates from the SSD primary vertex in the target. RECON Vees sharing the same  $xz$  projections are arbitrated on the basis of their  $\chi^2/\text{DOF}$ .

This type of Vee is not used in FOCUS analyses.

#### 4.4 P34 Vees

P34 Vees are Vees which decayed between P2 and P3 in the magnetic field of M2. Because their decay region is the most downstream considered, they are the Vee category with the highest momentum.

P34 Vees are reconstructed using hits in P3 and P4 which have not already been used both by the general MPWC pattern reconstruction and by the hits used in the RECON Vee category. Because the MPWC hits can be erroneously pre-assigned to another track category, the reconstruction efficiency for P34 Vees is not high. Track projections are formed in the  $xz$  (non-bend) plane and checked two at a time for intersecting between P2 and P3. Projections which don't intersect in this region are discarded. The projections from the U-view, V-view, and Y-view are formed and matched to the X projections to form tracks. In order to determine the unknown momenta of the two station tracks, it is necessary to further constrain the Vee vector to originate from the SSD primary vertex.

This type of Vee is not used in FOCUS analyses.

#### 4.5 One-link SSD Vees

One-link SSD Vees are reconstructed from the combination of a linked SSD and a MPWC track with an unlinked SSD track. These are  $K_S^0$  and  $\Lambda^0$  which decayed before the second SSD station, but for which one of the decay prongs falls out of the M1 geometrical acceptance and therefore is not found in the PWC.

The linked SSD to MPWC track and the unlinked SSD track are required to make a good space vertex with a confidence level greater than 1%. A primary vertex is used as a constraint. The significance of separation between the primary and Vee decay vertex ( $L/\sigma_L$ , is computed and it is required to have  $L/\sigma_L > 10$ . Also the primary-secondary vector is required to lie in the plane

of the two decay prongs. By knowing the momentum of the linked track, the primary-secondary direction and the unlinked track direction, it is possible to balance the transverse momentum and compute the total momentum of the unlinked track (there is no two-fold ambiguity in the kinematics). Finally, the invariant mass of the two tracks is computed for the  $K_S^0$  hypothesis and for the  $\Lambda^0$  hypothesis. In the  $K_S^0$  case no Čerenkov requirements in the two prongs are imposed, while in the  $\Lambda^0$  case the linked prong is identified by the Čerenkov algorithm [6] to have a light pattern more consistent with a proton hypothesis than a pion hypothesis. The  $\Lambda^0$  candidates where the pion is linked and the proton is unlinked are not reconstructed, since this kind of Vee contained very little signal over an overwhelming background. These Vees have a  $K_S^0$  mass resolution of  $4.7 \text{ MeV}/c^2$ .

#### 4.6 MIC Vees

MIC Vees have the decay vertex between the second and the fourth (last) SSD station. The reconstruction algorithm starts by projecting unlinked MPWC tracks backward onto the SSD detector and by searching for unused hits in the last two stations. If one or more matching triplets of hits are found, the parameters of the track are recomputed by a global fit which uses both the SSD and the MPWC hits. The new reconstructed tracks are then checked two at a time to see if they originate from the same vertex in space, and a cut on the distance of closest approach (DCA) is imposed. Candidate Vees sharing one prong are arbitrated on the basis of minimum DCA. The  $K_S^0$  mass resolution for this category is  $4.4 \text{ MeV}/c^2$ .

This type of Vee is not used in FOCUS analyses.

#### 4.7 Single-linked MPWC Vees

Single-linked MPWC Vees share the same decay region of the M1 Vees (between the SSD detector and P0), but are composed of one linked SSD to MPWC track and one unlinked MPWC track. The reconstruction algorithm is essentially the same as for the M1 Vees, and they are divided into three subcategories: *track-track*, *track-stub*, and *stub-stub*. For the  $K_S^0$  reconstruction there was too much background in these categories and they were never used. However, for the  $\Lambda^0$  they were very important particularly when the  $\Lambda^0$  was a decay product of a  $\Xi^-$  or a  $\Omega^-$ .

#### 4.8 Arbitration of Vee types

In high multiplicity events it is possible for a track to be found in more than one Vee category. This occurs when one or both of the daughter tracks in a Vee are found in other Vee candidates. The Vee candidates are arbitrated so that a single MPWC track is used just once in forming a Vee. In order for a Vee to be arbitrated it must first have passed the basic requirements such as being within the mass windows and satisfying the normalized mass cuts and it must have a track shared with another Vee that satisfies the same basic conditions. The decision to keep a Vee is made with the following criteria.

- Two SSD Vees sharing a microstrip segment are arbitrated based on which Vee has the smaller distance of closest approach at the decay vertex location.
- Two M1 *track-track* Vees sharing a MPWC track are arbitrated based on which Vee has the smaller distance of closest approach at the decay vertex location.
- M1 *track-track* Vees are always selected over M1 *track-stub* Vees.
- Two M1 *track-stub* Vees sharing a MPWC track are arbitrated based on which Vee has the smaller  $\chi^2/\text{DOF}$  of the fit.
- M1 *track-stub* Vees are always selected over M1 *stub-stub* Vees.
- Two M1 *stub-stub* Vees sharing a MPWC track are arbitrated based on which Vee has the smaller  $\chi^2/\text{DOF}$  of the fit.

#### 4.9 Vee Refit

Vees are reconstructed with only a rough knowledge of their actual production vertex. For the purposes of track finding the assumption is made that the tracks originate at the primary vertex (see Fig. 4). When a secondary charmed particle vertex is identified, then the Vee is refit to the true production vertex. This refit slightly improves the Vee production angle and the Vee mass.

Six histograms of  $K_S^0$  Vee types are presented in Fig. 5. The histograms are all plotted on the same mass scale and were made from the same small data sample (approximately 0.5% of the total). The (*M1 stub-stub*) Vees have the most background and the poorest mass resolution. The (*M1 track-track*) and (*M1 track-stub*) Vees are the most common categories. The (*MIC*) Vees have the least background, but the yield is comparatively low. The (*SSD*) Vees have the best mass resolution, but can have considerable background since

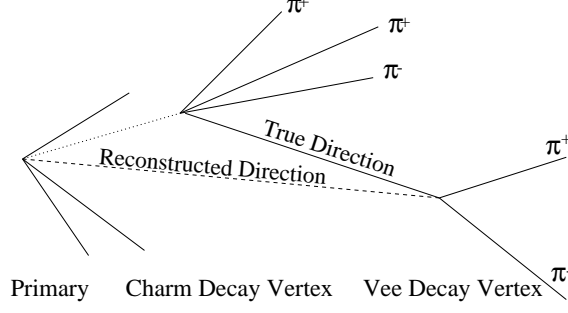


Fig. 4. A sketch of the charmed particle decay  $D^+ \rightarrow K_S^0 \pi^+ \pi^+ \pi^-$  where the  $K_S^0 \rightarrow \pi^+ \pi^-$  is presented to display the need for a Vee refit. The  $K_S^0$  is first reconstructed to originate from the primary vertex, but a refit is necessary when it is reassigned to come from a new vertex.

the decay occurs close to the interaction region. The (*One-link*) Vees also have good mass resolution due to their very low momentum, but these Vees have considerable background.

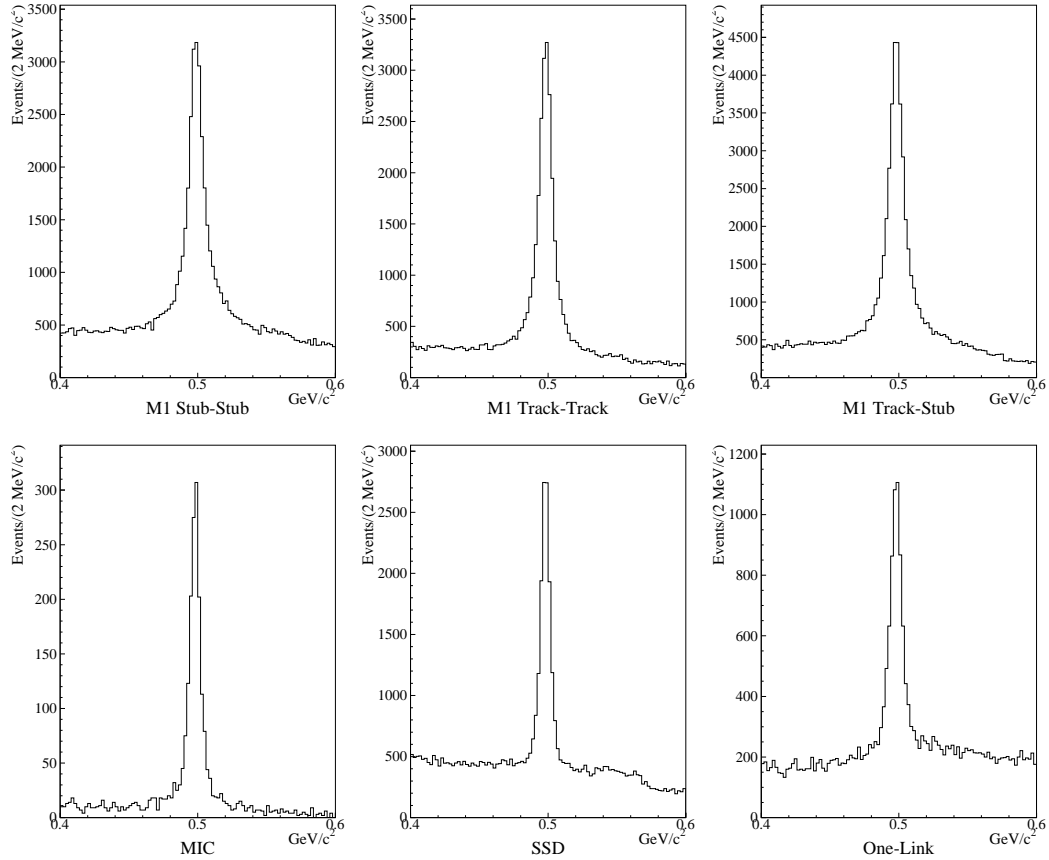


Fig. 5. Histograms of a sample of six categories of  $K_S^0$ 's which are used in the analysis. The dominant categories in charm decays are the (*M1 track-track*) and (*M1 track-stub*) Vees. The categories with the best resolution are *MIC*, *SSD*, and *One-link* Vees.



Nine histograms of  $\Lambda^0$  Vee types are plotted in Fig. 6. The data represents about 0.5% of the total  $\Lambda^0$  yield. For the  $\Lambda^0$  decays it is useful to retain the (*Single-linked*) categories, since  $\Xi^-$ 's and  $\Omega^-$ 's decay to  $\Lambda^0$ 's and occasionally the proton in the  $\Lambda^0$  decay is erroneously linked with the  $\Xi^-$  or  $\Omega^-$  track segment in the SSD.

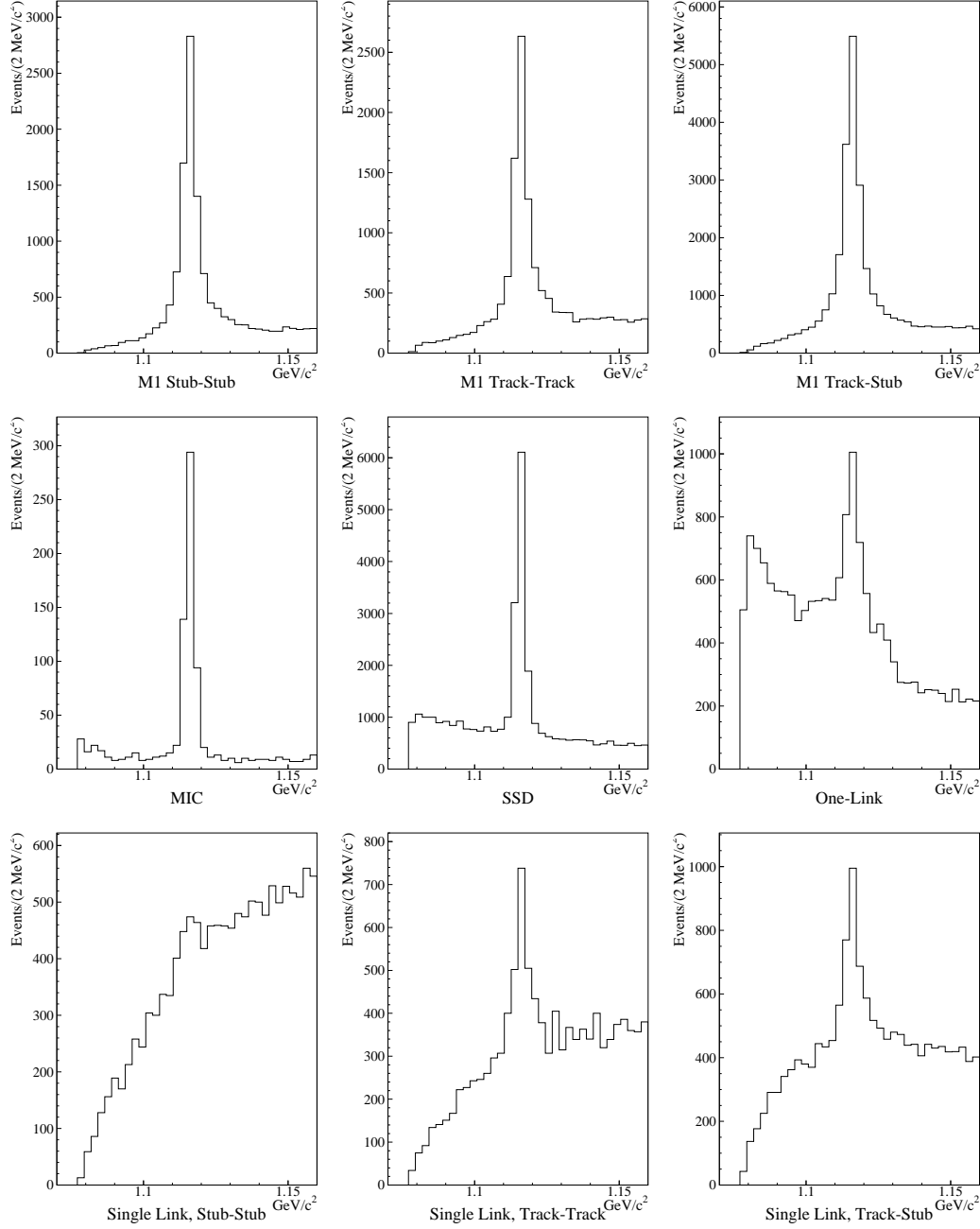


Fig. 6. Histograms of a sample of nine categories of  $\Lambda^0$ 's which are used in the FOCUS analyses. The final row of Single-linked  $\Lambda^0$ 's are not used in charm analyses involving direct charm decays to  $\Lambda^0$ 's, but account for almost 15% of the  $\Xi^-$ 's and  $\Omega^-$ 's decays.

## 5 Kinks

The term “Kink” refers to the topology where one charged particle decays to another charged particle and a neutral particle. The neutral particle is undetected in the tracking detectors.

A schematic of a Kink decay is given in Fig. 7. The parent particle with measured direction cosines,  $\alpha, \beta, \gamma$  and with mass,  $m_p$ , decays to particles  $m_1$  and  $m_2$ . Particle  $m_1$  has its momentum and direction cosines measured. Particle 2 is neutral and goes undetected in the spectrometer. Through kinematic constraints and by assuming its mass the parent momentum is calculated to within a twofold ambiguity.

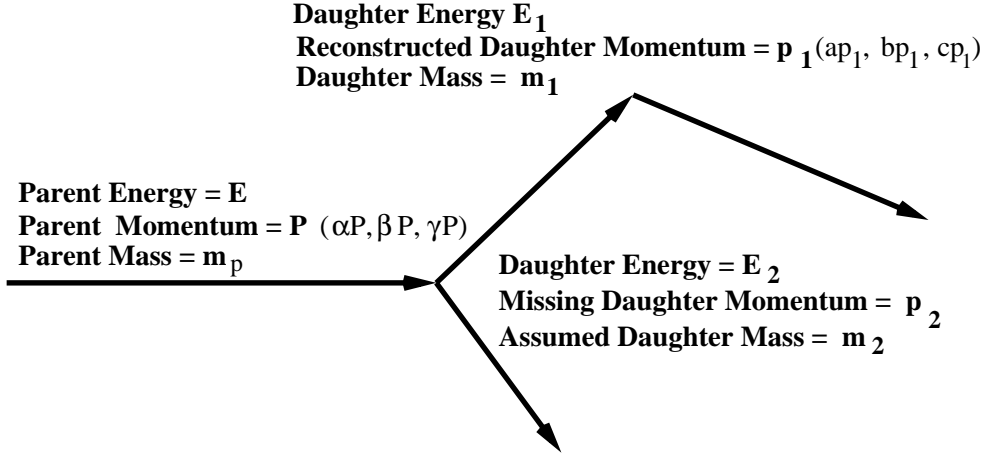


Fig. 7. A sketch of the Kink decay process where a parent particle decays to two tracks where one track is completely measured and the other track information is unknown. The direction of the parent track is known, but its momentum is unknown. Through kinematics the momentum of the parent particle can be calculated to within a twofold ambiguity.

The momentum of  $p_2$  is determined through conservation of momentum,

$$\mathbf{p}_2 = (\alpha P - ap_1, \beta P - bp_1, \gamma P - cp_1) \quad (2)$$

and the square of the energy of  $E_2$  is given by

$$E_2^2 = (E - E_1)^2 = p_2^2 + m_2^2 \quad (3)$$

Substituting the expression for  $\mathbf{p}_2^2$  we obtain

$$(m_p^2 + m_1^2 - m_2^2) + 2Pp_1(\alpha a + \beta b + \gamma c) = 2EE_1 \quad (4)$$

Squaring this equation, substituting  $P^2 = E^2 - m_p^2$ , and solving for  $P$ , we find

$$P = \frac{MC \pm \sqrt{M^2 C^2 - (1 - C^2)(m_p^2 - M^2)}}{(1 - C^2)} \quad (5)$$

where  $M = \frac{m_p^2 + m_1^2 - m_2^2}{2E_1}$ ,  $C = \frac{p_1(a\alpha + b\beta + c\gamma)}{E_1}$ , and  $P > 0$ . Thus, we find the twofold ambiguity.

The three decays  $\Sigma^+ \rightarrow p\pi^0$ ,  $\Sigma^+ \rightarrow n\pi^+$ , and  $\Sigma^- \rightarrow n\pi^-$  are reconstructed using the *Kink* algorithm. It should be noted that the  $\Sigma^+(suu)$  and the  $\Sigma^-(sdd)$  are *not* charge conjugate partners and that the 8 MeV/ $c^2$  difference in their masses is important to include in the algorithm. The  $\Sigma^+$  decays weakly to  $p\pi^0$  51.6% of the time and to  $n\pi^+$  48.4% of the time. The  $\Sigma^-$  decays to  $n\pi^-$  essentially 100% of the time. A complete list of the Kink candidates considered is given in Table 2. The fraction of the meson decays that we would recover from the Kink algorithm is insignificant compared to the prevalence of the non-decaying ones. We therefore concentrated on the hyperon decays,  $\Sigma$ 's,  $\Xi$ 's, and  $\Omega$ 's. Initially, we concentrated on the  $\Sigma$  decays. The decays  $\Xi^- \rightarrow \Lambda\pi^-$ ,  $\Omega^- \rightarrow \Lambda K^-$ , and  $\Omega^- \rightarrow \Xi^0\pi^-$  will be further considered in Section 6.

Table 2

Decay topologies considered in the Kink algorithm.

Type	Decay	$c\tau(\text{cm})$	Comments
1	$K^- \rightarrow \mu^- \nu$	371.3	muon identified
2	$\Sigma^+ \rightarrow n \pi^+$	2.396	neutron energy found in hadron calorimeter
3	$K^- \rightarrow \pi^- \pi^0$	371.3	
4	$\Sigma^+ \rightarrow p \pi^0$	2.396	$p$ identified by Čerenkov
5	$\Sigma^- \rightarrow n \pi^-$	4.434	neutron energy found in hadron calorimeter
6	$\pi^- \rightarrow \mu^- \nu$	780.45	muon identified
7	$\Xi^- \rightarrow \Lambda \pi^-$	4.91	
8	$\Omega^- \rightarrow \Lambda K^-$	2.46	$K$ identified by Čerenkov
9	$\Omega^- \rightarrow \Xi^0 \pi^-$	2.46	

The Kink algorithm begins by looping over each unlinked microstrip track that points into the M1 aperture and by pairing it with every unlinked MWPC track which also points into the M1 aperture. MWPC tracks used in Vee can-

didates are not considered. A preliminary Kink vertex location is determined by intersecting the microstrip and MWPC tracks in the  $xz$  plane. This choice provides a rough estimate of the  $x$  and  $z$  location, which is required to be downstream of the last microstrip station and upstream of P0.

If the MWPC track passes through all five MPWCs, then its momentum is already determined from M2 and it can be traced through the field of M1 to the estimated Kink  $z$  position. If the Kink  $z$  coordinate is upstream of M1, then the  $y$  distance between the projected 5-chamber track and the microstrip track is compared and required to be less than 2.5 mm. This helps eliminate spurious Kink candidates. The parent momentum can only be calculated by making a particular decay hypothesis and by solving the kinematic equations. This involves assuming the parent ( $\Sigma^\pm$ ) and daughter masses (including the missing neutral daughter) and balancing the momentum transverse to the parent direction. This results in a two-fold ambiguity in the parent momentum.

If the Kink  $z$  position is within M1, then the ambiguity can be broken and a unique solution is found. The MWPC track is traced upstream to the  $z$  of the Kink. The  $x$  and  $y$  coordinates of the Kink are then given by the traced position of the track at this  $z$ . The microstrip track is then traced downstream through M1 to the Kink position. The trace is iterated several times, using trial momenta, until a momentum is found which best traces the microstrip track to the Kink vertex. The transverse momentum is balanced and the kinematic equations are solved. If there are two physical solutions for the parent momentum, then the one nearest to the momentum calculated by the iterative trace is used. In theory, one could avoid solving the Kink kinematic equations for decays in the magnetic field by simply using the microstrip trace momentum, however often very little magnetic field is traced through and the resolution on the microstrip track curvature (momentum) is not well defined. For these reasons the kinematic solutions were always used to determine the momentum.

For 3-chamber MWPC tracks we consider only the case where the Kink position is upstream of M1. The  $x$  and  $y$  positions of the microstrip track at the previously estimated Kink  $z$  position are used as the Kink vertex location. An iterative trace procedure, similar to the one discussed above, is used to find the best momentum for the 3-chamber track. Unfortunately, a two-fold ambiguity exists in the parent momentum calculation.

All putative Kinks are reconstructed according to all three decay hypotheses (types 2, 4, and 5) from Table 2. Some hypotheses are rejected on the basis of particle identification of the charged daughter or on the basis of calorimetry information. Charged particle identification is made by re-running the Čerenkov code with the momentum determined from the Kink reconstruction in order to obtain a new Čerenkov identification estimate (*i.e.* the momentum changes).

For the  $\Sigma^+ \rightarrow p\pi^0$  hypothesis the Čerenkov light pattern is required to be more consistent with a proton assumption than the pion assumption by a factor of 7. For the  $\Sigma^+ \rightarrow n\pi^+$  and  $\Sigma^- \rightarrow n\pi^-$  hypotheses the pion is required to not be consistent with being an electron, kaon, or proton and the neutron must impact the hadron calorimeter. The neutron must deposit sufficient energy,  $E$ , surrounding the point where the neutron is expected to strike the calorimeters and must satisfy  $0.3 < E/p < 2.0$ , where  $p$  is the momentum of the neutron calculated from the Kink kinematic equations. A detailed description of the FOCUS hadron calorimeter and its performance is found in Reference 7.

There is no method to plot the mass of the reconstructed Kinks directly because of the assumed mass constraint in the algorithm. To show the success of our algorithm we present the invariant mass plots in Fig. 8 for  $\Lambda_c^+ \rightarrow \Sigma^- \pi^+ \pi^+$  where the  $\Sigma^-$  is reconstructed through the  $n\pi^-$  channel and for  $\Lambda_c^+ \rightarrow \Sigma^+ \pi^+ \pi^-$  where the  $\Sigma^+$  is reconstructed through the  $p\pi^0$  channel and through the  $n\pi^+$  channel. Care has been taken to weight the cases where there are two solutions such that the yields in the caption for Fig. 8 are correct.

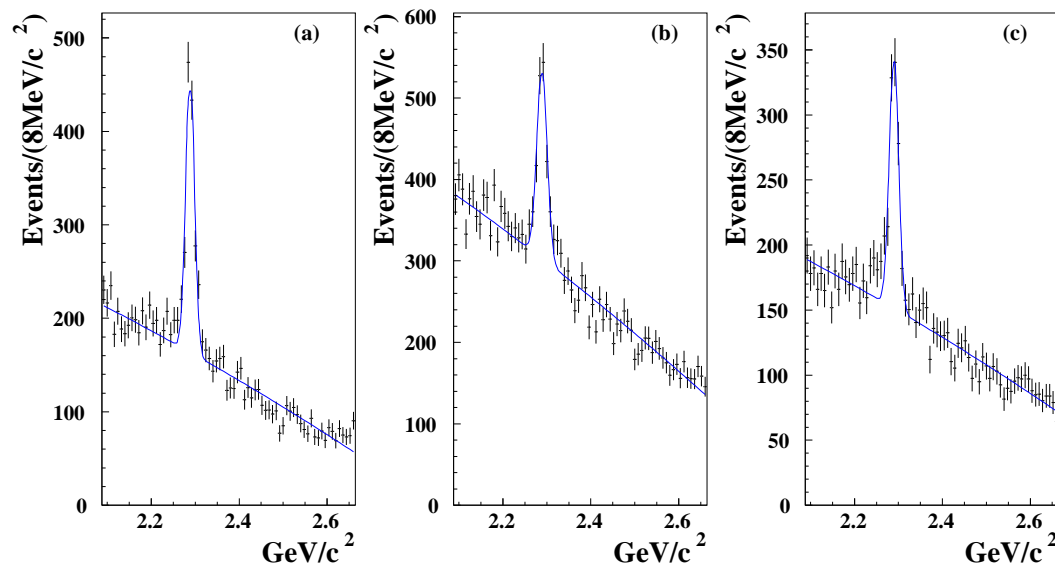


Fig. 8. Three invariant mass plots for the decays (a)  $\Lambda_c^+ \rightarrow \Sigma^+ \pi^+ \pi^-$  where  $\Sigma^+ \rightarrow p\pi^0$  with a yield of  $915 \pm 50$  events, (b)  $\Lambda_c^+ \rightarrow \Sigma^+ \pi^+ \pi^-$  where  $\Sigma^+ \rightarrow n\pi^+$  with a yield of  $854 \pm 65$  events, and for (c)  $\Lambda_c^+ \rightarrow \Sigma^- \pi^+ \pi^-$  where  $\Sigma^- \rightarrow n\pi^-$  with a yield of  $654 \pm 42$  events.

## 6 $\Xi^-$ 's and $\Omega^-$ 's

The  $\Xi^- \rightarrow \Lambda^0 \pi^-$  and  $\Omega^- \rightarrow \Lambda^0 K^-$  decays are reconstructed via several techniques. The  $\Xi^-$ 's and  $\Omega^-$ 's decaying upstream of the silicon microstrip de-

tector are reconstructed differently than those decaying downstream of the microstrip. If a Vee is not found, or if the  $\Lambda^0$ - track vertex is located downstream of the Vee vertex (*i.e.* due to poor vertex resolution in the event), then we use a technique referred to as ‘multivees’ where there are three unlinked tracks. Finally, if no fully reconstructed  $\Xi^-$  or multivee is found, then we use a Kink algorithm to find  $\Xi^- \rightarrow \Lambda^0 \pi^-$  where the  $\Lambda^0$  is unidentified. This algorithm is needed to reconstruct the  $\Xi^-$  when  $\Lambda^0 \rightarrow n \pi^0$ . Each of these techniques will be described below.

The fully reconstructed algorithm uses a common set of requirements to select Vees as  $\Lambda^0$ 's. The Vee daughter track with the highest momentum is considered the proton for the  $\Lambda^0$  hypothesis and the Čerenkov algorithm is executed using momenta of the Vee tracks as determined by the Vee algorithm.

### 6.1 Upstream Reconstructed $\Xi^-$ 's and $\Omega^-$ 's

*Upstream*  $\Xi^-$ 's and  $\Omega^-$ 's are those which decay upstream of the first microstrip station (*i.e.* within the target or between the target and the microstrip detector). They are also referred to as ‘Type 1’ decays. A schematic of a typical  $\Xi^-$  decay in the category is presented in Fig. 9.

Linked MWPC tracks are paired with each  $\Lambda^0$  Vee which satisfies the  $\Lambda^0$  hypothesis. Upstream decays are reconstructed by intersecting the  $\Lambda^0$  vector and the MWPC track and by demanding that the confidence level of this vertex be greater than 1% and that the  $\Xi^-/\Omega^-$  be consistent with originating from a production vertex further upstream. The distance between the production vertex and the  $\Xi^-/\Omega^-$  decay vertex is defined as  $L$ . The track is assigned the pion mass to form the invariant mass for  $\Xi^-$  hypothesis and is assigned the kaon mass for the  $\Omega^-$  hypothesis. There are two requirements which are used to significantly improve the signal-to-noise for these  $\Xi^-/\Omega^-$  signals. The first is the *significance of separation* of the  $\Xi^-/\Omega^-$  decay vertex from its production vertex. and the second is the isolation of the  $\Xi^-/\Omega^-$  decay vertex from other tracks.

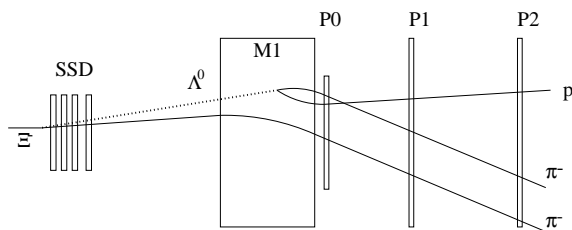


Fig. 9. A schematic drawing in the bend view of the spectrometer of a  $\Xi^-$  decay which occurs upstream of the silicon strip detector (SSD). Only the front part of the spectrometer is displayed.

The *significance of separation* of the  $\Xi^-/\Omega^-$  decay vertex from its production vertex is defined as the quantity  $L/\sigma_L$ , where  $\sigma_L$  is the error on  $L$ . By increasing the cut on  $L/\sigma_L$  (i.e.  $L/\sigma_L > 1, 2, 3$ , etc.) one obtains a cleaner sample. The basic algorithm requires  $L/\sigma_L > 0$ .

The isolation of the  $\Xi^-/\Omega^-$  decay vertex from other tracks is tested by attempting to place other tracks in the vertex and by refitting it. A cleaner signal is obtained by requiring that the confidence level from the fit to the new vertex be less than a certain value. Invariant mass plots for upstream decays for the  $\Lambda\pi^-$  and  $\Lambda K^-$  combinations are presented in Fig. 10. Note that there is considerable background under the  $\Omega^-$  signal which is almost entirely due to pion particle misidentification from the  $\Xi^- \rightarrow \Lambda\pi^-$  decays. One should also note that  $\Omega^-$  yield is about a factor of 20 less than the  $\Xi^-$  yield.

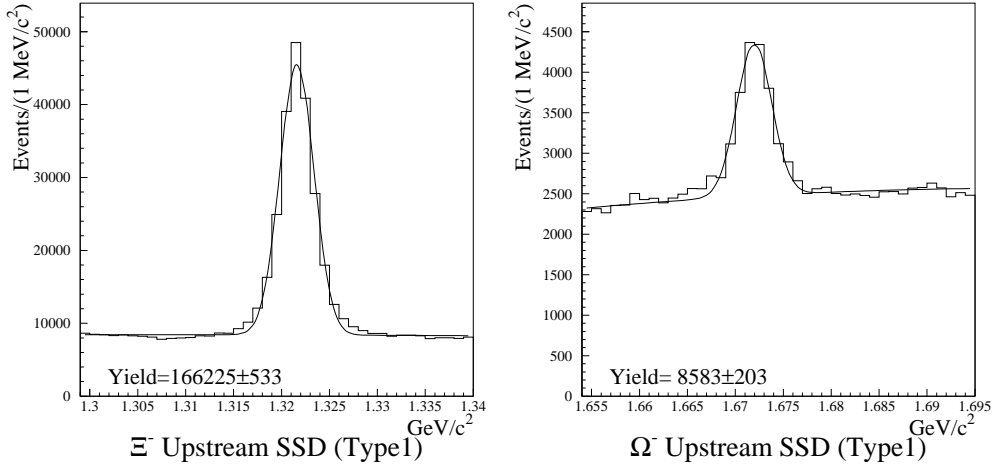


Fig. 10. The invariant mass plots for the  $\Lambda\pi^-$  and the  $\Lambda K^-$  combinations for the category where the decays occurs in front of the SSD detector. The plots represent the full FOCUS data sample.

## 6.2 Downstream Reconstructed $\Xi^-$ 's and $\Omega^-$ 's

*Downstream*  $\Xi^-$ 's and  $\Omega^-$ 's are those which decay downstream of the last microstrip plane and upstream of the first MWPC plane. They are also referred to as 'Type 2' decays. A schematic of a typical  $\Xi^-$  decay in this category is presented in Fig. 11. The decay distance for this category is more than three meters along the beam direction. A very important advantage to these decays is that the  $\Xi^-/\Omega^-$  leaves a track in the microstrip detector before decaying. This track can in turn be used for finding charmed particle baryon decay vertices.

The reconstruction algorithm begins by pairing each  $\Lambda^0$  with every unlinked

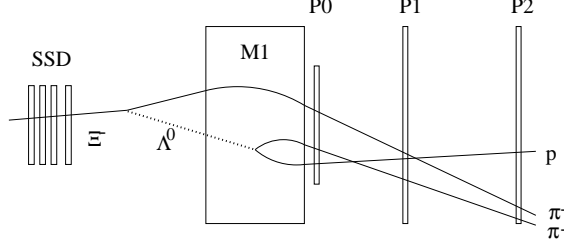


Fig. 11. A schematic drawing in the bend view of the spectrometer of a  $\Xi^-$  decay which occurs downstream of the silicon strip detector (SSD). Only the front part of the spectrometer is displayed.

MWPC track in the event. An estimate is made for the  $\Lambda^0$ -track vertex by computing the  $z$  intersection of the  $\Lambda^0$  vector and the track in the non-bend view ( $xz$ ) plane. If this vertex is downstream of P0 or more than 50 cm upstream of the target, then the combination is rejected. An estimate for the  $x$  and  $y$  positions of the vertex is given by the  $x$  and  $y$  of the  $\Lambda^0$  vector at the given  $z$  of the vertex (because the  $\Lambda^0$  is neutral its path is not deflected by the field of M1). The unlinked track is next traced through the magnetic field of M1 to the position of the putative vertex. If the track is 3-chamber, then an iterative procedure is used whereby the track is assigned a different momentum for each iteration until a good trace is made to the given vertex. A better determination of the vertex  $z$  position is made by computing the distance of closest approach between the  $\Lambda^0$  vector and track. (This iteration is important because the track can pass through only one side of the magnet making fringe field corrections more significant.)

Next, the microstrip track of the candidate charged  $\Xi^-/\Omega^-$  is found. The sum of the momentum vectors of the  $\Lambda^0$  and the track are used to form a candidate  $\Xi^-/\Omega^-$ . Unlinked microstrip tracks are used and an attempt is made to match each one with the candidate  $\Xi^-/\Omega^-$ . If the  $\Lambda^0$  under consideration is a single-link Vee, then the Vee-linked microstrip is used. Each candidate microstrip track is traced downstream to the  $\Lambda^0$ -track vertex; if the vertex is within the field of M1, then the magnetic trace is used otherwise the microstrip vector is simply extrapolated to the vertex. Because the microstrip track has much better position resolution than does the Vee, a better vertex position can now be determined. The new  $z$  position is defined as the  $z$  where the microstrip track and the MWPC track make their closest approach. If the  $z$  position is downstream of P0 or upstream of the target, the microstrip track is rejected as a candidate. Also, the  $\Xi^-/\Omega^-$  vertex is required to be upstream of the  $\Lambda^0$  vertex.

To remove spurious matches in this algorithm, a cut is made on the candidate vertex. The candidate vertex is calculated in two ways: the point where the  $\Lambda^0$  and the MWPC track make their closest approach, and the point where the microstrip track and the MWPC track make their closest approach. A cut



is made on the transverse distance (in the  $x$ - $y$  plane) between these two putative vertices. The second quantity on which a cut is applied is the difference between the  $x$  and  $y$  slopes of the microstrip track and slopes given by the sum of the  $\Lambda^0$  and the MWPC track momentum vectors. The  $x$  and  $y$  slopes must agree to within 4 milliradians of the momentum vectors.

The MWPC track is assigned a pion mass for the  $\Xi^-$  hypothesis and is assigned a kaon mass for the  $\Omega^-$  hypothesis. For the  $\Omega^-$  candidates, the MWPC track is required to be identified by the Čerenkov counters as being consistent with a kaon hypothesis.

Invariant mass plots for downstream decays for the  $\Lambda\pi^-$  and  $\Lambda K^-$  combinations are presented in Fig. 12. In this region one finds that the  $\Omega^-$  yield is a factor of 30 lower than the  $\Xi^-$  yield. The ratio of the  $\Omega^-$  yield to the  $\Xi^-$  yield is reduced downstream of the SSD detector due to the shorter  $\Omega^-$  lifetime relative to the  $\Xi^-$ .

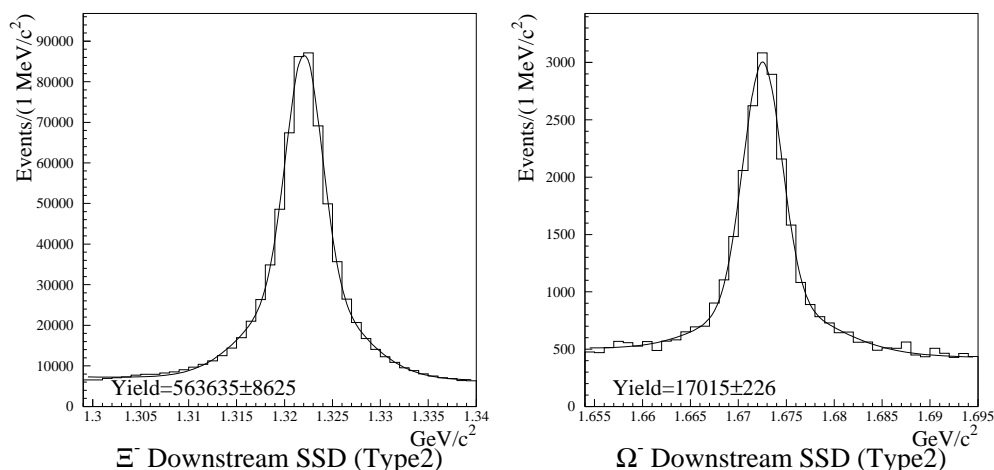


Fig. 12. The invariant mass plots for the  $\Lambda\pi^-$  and the  $\Lambda K^-$  combinations for the category where the decays occurs downstream of the SSD detector. The plots are for the full FOCUS data sample.

### 6.3 Multivees

A ‘multivee’ is composed of three unlinked MWPC tracks and one unlinked SSD track. A schematic drawing of a multivee decay is presented in Fig. 13. While the category was designed to select three prong decays such as  $K^- \rightarrow \pi^- \pi^- \pi^+$ , it has proven to be useful in recovering  $\Xi^-$  and  $\Omega^-$  decays where the  $\Lambda^0$  decay vertex is close to the  $\Xi^-$  decay vertex. It also works well in reconstructing Vees from  $\Xi^-$  decays which open in the vertical plane of the magnet.

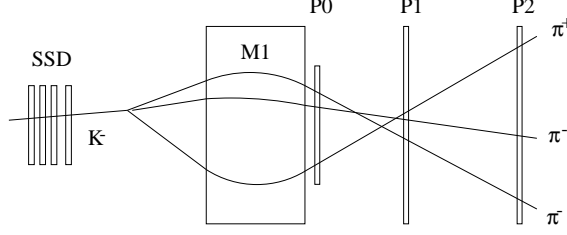


Fig. 13. A schematic bend view drawing of the decay of the  $K^- \rightarrow \pi^+ \pi^- \pi^-$  using three unlinked MWPC tracks and one unlinked SSD track.

Initially, three unlinked MWPC tracks are intersected in the  $xz$  view and an unlinked SSD track with the closest distance of approach at the  $xz$  vertex is selected as a match. The algorithm is separated into decays which occur upstream of M1 and within M1.

If the decay vertex is upstream of the M1 magnet, then the SSD track is extrapolated in  $z$  to the vertex and each of the stubs are traced to the SSD  $y$  vertex position. If there are five chamber tracks, then they are swum upstream and intersected with the SSD track to find a better vertex position.

If the decay occurs within the magnetic field, then there must be at least one five chamber track. The vertex of the three unlinked MWPC tracks is found in the  $xz$  plane and the  $y$  location of the vertex is determined by swimming the tracks to the  $z$  location. If more than one five chamber track exists, then the  $z$  location is determined using the combined  $x + y$  information. All remaining unlinked stubs are traced to the  $yz$  vertex and their momentum is calculated. Next, the sum of the three unlinked track momenta is found and assigned to the microstrip track. This unlinked SSD track is now traced downstream to the  $z$  vertex. Successful candidates must be near the vertex of the three unlinked tracks and must agree in slope to within 4 milliradians in both the  $x$  and  $y$  views to the combined momentum vectors of the three tracks.

In Fig. 14 the invariant mass distributions for  $\pi^+ \pi^+ \pi^-$ ,  $p \pi^- \pi^-$ , and  $p K^- \pi^-$  combinations are presented. While the charge kaon decay events are not used in our analysis packages, the  $\Xi^-$  decays and  $\Omega^-$  decays are used.

#### 6.4 Kinks

The algorithm for reconstructing the  $\Xi^- \rightarrow \Lambda^0 \pi^-$  decays as presented in Fig. 15 is similar to the  $\Sigma$  decays discussed in Section 5. Unfortunately, there is no good technique to reduce the sample with additional constraints such as energy in the calorimeter or with Čerenkov cuts. For this reason we chose to only reconstruct events where the  $\Xi^-$  decay occurred within the magnetic field of M1. There are three advantages to using this subsample. First, the

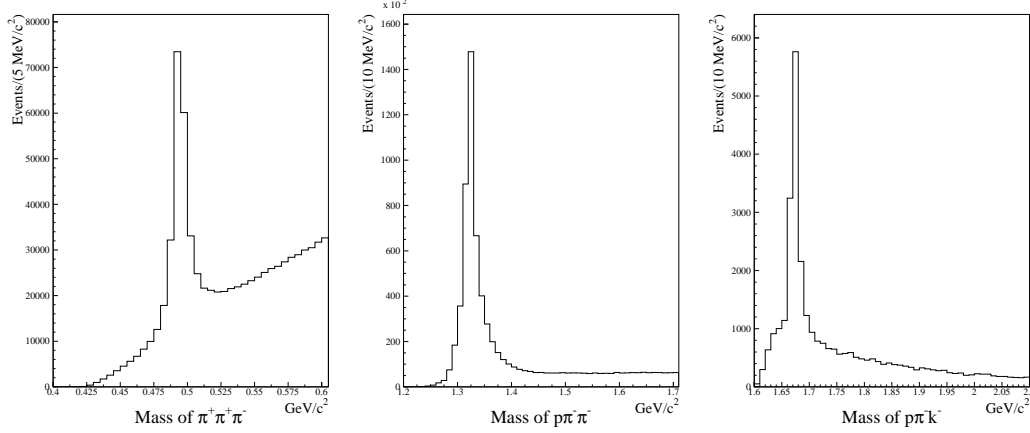


Fig. 14. Invariant mass distributions for  $\pi^+\pi^+\pi^-$ ,  $p\pi^-\pi^-$ , and  $pK^-\pi^-$  combinations. Signals for  $K^+ \rightarrow \pi^+\pi^+\pi^-$ ,  $\Xi^- \rightarrow \Lambda^0\pi^-$  where  $\Lambda^0 \rightarrow p\pi^-$ , and  $\Omega^- \rightarrow \Lambda^0K^-$  where  $\Lambda^0 \rightarrow p\pi^-$  are clearly evident.

reconstructed pion or kaon is a five chamber track and its momentum is well defined by its passage through M2. Second, there is no two-fold ambiguity in this category as the  $\Xi^-$  also bends in the magnetic field. Third, the decays are well-separated from any material and the background from large multiple scatters is significantly reduced.

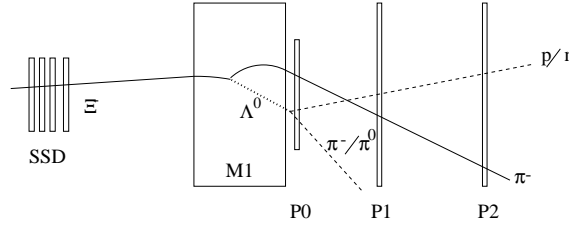


Fig. 15. A schematic bend view drawing for a  $\Xi^-$  decay inside of M1 where the  $\Lambda^0$  is not reconstructed.

## 6.5 $\Xi_c^+$ Mass Plots

Invariant mass plots from the full FOCUS data sample for the charmed particle decay  $\Xi_c^+ \rightarrow \Xi^-\pi^+\pi^+$  for each of the four categories discussed above are presented in Fig. 16. The mass plots were found with a significance of separation cut of  $L/\sigma_L > 4$  between the secondary and primary vertices.  $\Xi^-$ 's are selected such that there is no overlap between categories. Upstream  $\Xi^-$ 's or Type 1 decays have no overlap with the other categories because they decay before the SSD detector. Downstream  $\Xi^-$ 's or Type 2 decays are fully reconstructed and are the cleanest of the decays. If a Type 2 decay occurs in an event, the  $\Xi^-$  Kink and multivee algorithms are not run. The next cleanest category is the  $\Xi^-$  multivees. If a  $\Xi^-$  multivee is found, then the  $\Xi^-$  Kink

algorithm is not used.

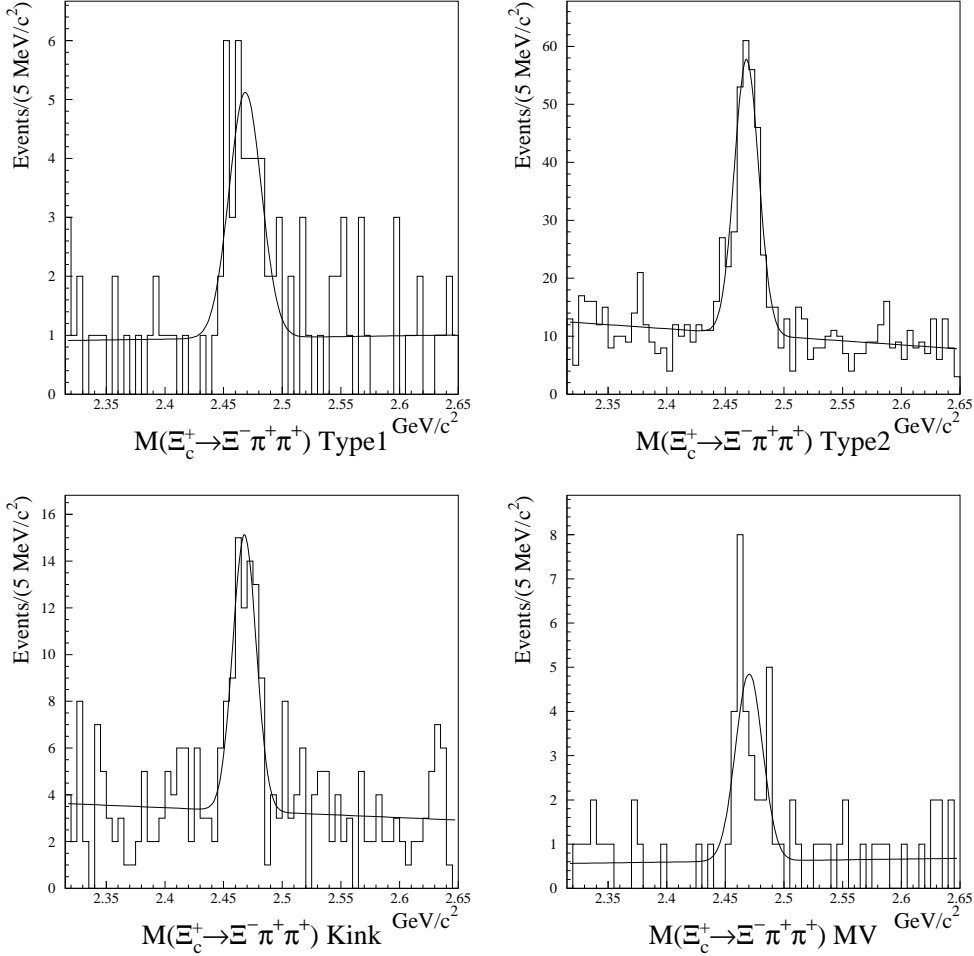


Fig. 16. Invariant mass plots for the charmed particle decay  $\Xi_c^+ \rightarrow \Xi^- \pi^+ \pi^+$  using type1 (upstream  $\Xi^-$ ) decays, using type 2 (downstream  $\Xi^-$ ) decays, using  $\Xi^-$  Kink decays, and using multivee decays.

From an inspection of Fig. 16, it is clear that the Type 2 category dominates the signal with  $246 \pm 20$  events, followed by the Kink category ( $59 \pm 9$  events), the Type 1 category ( $29 \pm 6$  events), and the multivee category ( $25 \pm 4$  events).

## 7 Summary and Conclusions

We have briefly described the tracking algorithms of FOCUS and how the high resolution silicon microstrip system is integrated with multiwire proportional chambers. Further, we have described the various techniques developed to reconstruct  $K_S^0$  and  $\Lambda^0$  decays in a multiparticle spectrometer. We have de-

scribed the two-fold ambiguity that occurs from  $\Sigma^+$  and  $\Sigma^-$  decays to a single charged particle and an unobserved neutral decay. Through these ‘Kink’ kinematics we are able to observe charm baryon decays. Finally, we have combined the techniques of Vees and Kinks and used these techniques in the reconstruction of  $\Xi^-$  and  $\Omega^-$  decays. We believe the techniques described in this paper will prove useful to future experiments and may serve to show what is possible in multipurpose spectrometers.

## Acknowledgments

We wish to acknowledge the assistance of the staffs of Fermi National Accelerator Laboratory, the INFN of Italy, and the physics departments of the collaborating institutions. This research was supported in part by the U. S. National Science Foundation, the U. S. Department of Energy, the Italian Istituto Nazionale di Fisica Nucleare and Ministero dell’Università e della Ricerca Scientifica e Tecnologica, the Brazilian Conselho Nacional de Desenvolvimento Científico e Tecnológico, CONACyT-México, the Korean Ministry of Education, and the Korean Science and Engineering Foundation.

## References

- [1] E687 Collaboration, P.L. Frabetti *et al.*, *Nucl. Instrum. Methods A* **320**, 519 (1992).
- [2] G. Bellini *et al.*, *Nucl. Instrum. Methods A* **252**, 366 (1986).
- [3] Luca Cinquini, Ph.D. thesis, University of Colorado, Boulder, Colorado, 1996.
- [4] D. Groom, *et al.*, *Eur. Phys. J.* **C15**, 1 (2000).
- [5] FOCUS Collaboration, J.M. Link *et al.*, *Phys. Lett. B* **485**, 62 (2000)
- [6] FOCUS Collaboration, J.M. Link *et al.*, submitted for publication to Nuclear Instruments and Methods; hep-ex/0108011.
- [7] V.Arena *et al.*, *Nucl. Instrum. Methods A* **434**, 271 (1999).